

## ORIGINAL ARTICLE

# Highly stable and efficient solid-state solar cells based on methylammonium lead bromide ( $\text{CH}_3\text{NH}_3\text{PbBr}_3$ ) perovskite quantum dots

Sawanta S Mali, Chang Su Shim and Chang Kook Hong

Easy processability and high stability are key features of methylammonium lead bromide ( $\text{CH}_3\text{NH}_3\text{PbBr}_3$ )-based perovskite solar cells. The main focus of the present work was to fabricate and evaluate the stability of  $\text{CH}_3\text{NH}_3\text{PbBr}_3$  quantum dot (QD)-based perovskite solar cells. We used an *ex situ* solution process to synthesize  $\text{CH}_3\text{NH}_3\text{PbBr}_3$  QDs and then successfully fabricated mesoscopic solid-state perovskite solar cells. We also studied the influence of different  $\text{CH}_3\text{NH}_3\text{PbBr}_3$  QD sizes and different hole-transporting materials (HTMs), 2,2',7,7'-tetrakis-(*N,N*-di-4-methoxyphenylamino)-9,9'-spirobifluorene (spiro-MeOTAD) and poly[bis(4-phenyl)(2,4,6-trimethylphenyl)amine] (PTAA), on the solar cell performance. The size of the  $\text{CH}_3\text{NH}_3\text{PbBr}_3$  QDs was controlled by the solution processing parameters. Our controlled results show that spiro-MeOTAD- and PTAA-based devices exhibited, respectively, an open-circuit voltage ( $V_{\text{OC}}$ ) of 0.991 and 1.091 V and a current density ( $J_{\text{SC}}$ ) of 11.68 and 12.05  $\text{mA cm}^{-2}$ , which resulted in an average power conversion efficiency (PCE) of 7.35 and 9.44% under a standard  $100 \text{ mW cm}^{-2}$  illumination without masking. Our best-performing cell, which contains the  $\text{FTO/BI-TiO}_2/\text{mp-TiO}_2+\text{CH}_3\text{NH}_3\text{PbBr}_3$  (~2-nm QDs)/PTAA/Au configuration shows the following results: open-circuit voltage ( $V_{\text{OC}}$ ) = 1.110 V, current density ( $J_{\text{SC}}$ ) = 14.07  $\text{mA cm}^{-2}$ , fill factor = 0.73 and an 11.40% PCE. Furthermore, the  $\text{CH}_3\text{NH}_3\text{PbBr}_3$ -based devices are stable for more than four months.

NPG Asia Materials (2015) 7, e208; doi:10.1038/am.2015.86; published online 14 August 2015

## INTRODUCTION

Methylammonium lead halide (MAPbX) (X=I, Br or Cl)-based perovskite solar cells (PSCs) open new approaches for the fabrication of efficient and stable solid-state dye-sensitized solar cells. The pioneering work on alkali-metal lead and tin halides was performed by Wells.<sup>1</sup> The chemical formula of the compound that he used was  $\text{CsPbX}_3$  (X=Cl, Br or I). However, 94 years later, D. Weber *et al.* successfully replaced cesium (Cs) with methylammonium cations ( $\text{CH}_3\text{NH}_3^+$ ) and studied various compositions of the first three-dimensional organic-inorganic hybrid perovskites by tuning their crystal structures and phases.<sup>2,3</sup> Specifically,  $\text{MAPbBr}_3$  perovskite shows the cubic phase I (*Pm3m*), tetragonal phase II (*I4/mcm*) and orthorhombic phase IV (*Pnma*,  $Z=4$ ) systems. This is a p-type semiconducting material with a direct band gap of 1.93–2.3 eV that corresponds to an absorption onset of  $\leq 550 \text{ nm}$ , which makes this material an excellent light harvester.<sup>4,5</sup> After successful synthesis of  $\text{CH}_3\text{NH}_3\text{PbI}_3$  perovskite quantum dots (QDs), Im *et al.* demonstrated a 6.5% power conversion efficiency (PCE) via the *ex situ* method.<sup>6</sup> Degradation of perovskite in a liquid electrolyte was solved by Gratzel *et al.* in 2013 using solid-state PSCs with a 13% PCE.<sup>7</sup>

The perovskite degradation problem has been nullified by implementing solid-state hole-transporting material (HTMs), for example, 2,2',7,7'-tetrakis-(*N,N*-di-*p*-methoxyphenyl-amine)-9,9'-spirobifluorene (spiro-MeOTAD).<sup>7</sup> Thus, for the last 2 years, methylammonium lead

halide perovskite semiconductors have enabled of low cost solution-processed photovoltaic technology. On average, the PCE is typically boosted to 16.6% (certified), with the highest reported efficiency of ~19.3% (uncertified) for a  $\text{CH}_3\text{NH}_3\text{PbI}_{3-x}\text{Cl}_x$  perovskite with a planar geometry and without an antireflective coating.<sup>8</sup>

Perovskite materials with different compositions have been successfully synthesized using *in situ*, *ex situ*, solvent engineering, compositional chemical management and vapor deposition techniques. Recently, Snaith *et al.* synthesized a mixed halide perovskite  $\text{CH}_3\text{NH}_3\text{PbI}_{3-x}\text{Cl}_x$  using the dual-source vapor deposition technique to fabricate planar heterojunction PSC.<sup>9</sup> An open-circuit voltage ( $V_{\text{OC}}$ ) of 1.07 V (the highest reported so far), a high current density ( $J_{\text{SC}}$ ) of 21.5  $\text{mA cm}^{-2}$ , and a 15.4% PCE were achieved. These results were achieved using the pinhole-free perovskite layer deposition technique, which enables thermal evaporation with a uniform HTM layer and a high diffusion length ( $L_{\text{D}}$ ; 1069 nm).<sup>9,10</sup> In addition, the  $V_{\text{OC}}$  of the perovskite material can be controlled with electron-transporting layers (ETLs) such as  $\text{TiO}_2$ ,  $\text{Al}_2\text{O}_3$  and Yttrium-doped  $\text{TiO}_2$  (Y- $\text{TiO}_2$ ).<sup>8,11</sup> Y. H. Hu discussed the state of the art of novel meso-superstructured solar cells that are based on an insulating ETL ( $\text{Al}_2\text{O}_3$ ) and a lead-free perovskite ( $\text{MASnI}_3$ ) for solar cell applications.<sup>12</sup> Recently, we have synthesized  $\text{CH}_3\text{NH}_3\text{PbI}_3$  perovskite nanoparticles from  $\gamma$ -butyrolactone solvent and successfully developed low temperature-processed one-dimensional  $\text{TiO}_2$  nanorod arrays

Polymer Energy Materials Laboratory, School of Applied Chemical Engineering, Chonnam National University, Gwangju, South Korea

Correspondence: Professor Dr CK Hong, Polymer Energy Materials Laboratory, School of Applied Chemical Engineering, Chonnam National University, Gwangju 500757, South Korea.

E-mail: hongck@chonnam.ac.kr

Received 20 January 2015; revised 28 March 2015; accepted 9 June 2015

with a 13.45% PCE.<sup>13,14</sup> Low temperature flexible PSCs have also been demonstrated by Yang *et al.* using phenyl- $\text{C}_{61}$ -butyric acid methyl ester (PCMB) as the HTM material, resulting in a 9.2% PCE.<sup>15</sup> However, a uniform deposition and thickness optimization of the phenyl- $\text{C}_{61}$ -butyric acid methyl ester is difficult to achieve.<sup>16</sup>

Recently, Seok *et al.* demonstrated a 16.2% PCE using solvent engineering and toluene drip casting treatment for perovskite materials.<sup>17</sup> This treatment helps to form an intermediate MAI-PbI<sub>2</sub>-dimethyl sulfoxide (DMSO) phase, which retards the rapid reaction between PbI<sub>2</sub> and MAI during the evaporation step and results in a highly pure crystalline  $\text{CH}_3\text{NH}_3\text{PbI}_3$  perovskite layer. However, these devices suffer from a low fill factor (FF) and hysteresis issues. The optimization of each layer is a major challenge for MAPbI<sub>3</sub>-based PSCs, but the hysteresis issue can be solved by varying the thickness of the mesoporous TiO<sub>2</sub> (mp-TiO<sub>2</sub>) layer. Seok *et al.* studied different compositions of methylammonium lead iodide (MAPbI<sub>3</sub>), formamidinium lead iodide (FAPbI<sub>3</sub>) and methylammonium lead bromide (MAPbBr<sub>3</sub>) as effective light harvesters for PSCs. From this study, they concluded that the incorporation of MAPbBr<sub>3</sub> into FAPbI<sub>3</sub> stabilized the perovskite phase of FAPbI<sub>3</sub> and improved the PCE of the solar cell. The authors<sup>18</sup> demonstrated a >18% PCE for mixed (FAPbI<sub>3</sub>)<sub>1-x</sub>(MAPbBr<sub>3</sub>)<sub>x</sub>, where  $x=0, 0.05$  or  $0.15$ . Therefore, a study of the bare MAPbBr<sub>3</sub> perovskite will open new opportunities in the architecture design of bilayer PSCs. Moreover, a high FF and high stability are the most important key features of MAPbBr<sub>3</sub>-based PSCs. It is well known that MAPbX<sub>3</sub> nanoparticles/QDs with sizes <10 nm enable the preparation of new device architectures that could further enhance solar cell performance and elucidate the perovskite operating mechanisms.<sup>19</sup> Therefore, MAPbBr<sub>3</sub> QDs-based PSCs open new approaches towards the development of stable and efficient solar cells. The optical properties of MAPbBr<sub>3</sub> and MAPbI<sub>3</sub> were investigated by Tanaka *et al.*<sup>20</sup> It was determined that for MAPbBr<sub>3</sub>, the exciton binding energy and the exciton Bohr radius were 76 meV and 20 Å, respectively; for MAPbI<sub>3</sub>, the exciton binding energy and exciton Bohr radius were 50 meV and 22 Å, respectively.<sup>21</sup> The absorption coefficients of MAPbBr<sub>3</sub> and MAPbI<sub>3</sub> are  $10^5 \text{ cm}^{-1}$  and  $>4.3 \times 10^5 \text{ cm}^{-1}$  (at 300 nm), respectively.

Cai *et al.* demonstrated a 3.04% PCE using poly[N-9-hepta-decanyl-2,7-carbazole-alt-3,6-bis(thiophen-5-yl)-2,5-dioctyl-2,5-dihydropyrrolo[3,4-]pyrrole-1,4-dione] (PCBTDP) as the HTM.<sup>22</sup> However, the  $V_{\text{OC}}$  can be tuned by the band gap and the HTM of the materials; the authors demonstrated a  $V_{\text{OC}}$  of 1.15 and 1.3 V for PCBTDP and *N,N'*-dialkylperylene diimide as the HTMs, respectively. Recently, E. Edri *et al.* demonstrated a 0.72% PCE with a  $V_{\text{OC}}$  of 1.06 V using phenyl- $\text{C}_{61}$ -butyric acid methyl ester as the HTMs<sup>23</sup> for MAPbBr<sub>3</sub> PSCs. Moreover, Seok *et al.* demonstrated band tuning by incorporating MAPbBr<sub>3</sub> (that is, Br doping) into MAPbI<sub>3</sub> to achieve a PCE of 12.3% and a  $V_{\text{OC}}$  of 1.13 V using polytriarylamine (PTAA) as the hole conductor.<sup>24</sup> The incorporation of MAPbBr<sub>3</sub> improved the  $V_{\text{OC}}$  and the current density from 0.87 to 1.13 V and from 5 to 18  $\text{mA cm}^{-2}$ , respectively.

Im *et al.* fabricated a planar MAPbBr<sub>3</sub> hybrid PSC using P3HT, PTAA and poly-indenofluoren-8-triarylamine (PIF8-TAA) as the HTMs. The MAPbBr<sub>3</sub> perovskites were synthesized in a dimethylformamide solvent, and the influence of H<sub>2</sub>O content was studied. The authors showed a 7.3%, 9.3% and 10.4% PCE with a  $V_{\text{OC}}$  of 1.09, 1.35 and 1.51 V for the P3HT, PTAA and PIF8-TAA HTMs, respectively.<sup>20</sup> To the best of our knowledge, there are no reports describing the synthesis of the MAPbBr<sub>3</sub> QDs with <3 nm sizes in either the dimethylformamide or DMSO solvents that are used for the solar cell application.

In the current study, we report the preparation of highly stable and high conversion efficiency mp-TiO<sub>2</sub>-based solid-state PSCs using MAPbBr<sub>3</sub> QDs. We synthesized highly crystalline MAPbBr<sub>3</sub> QDs with different sizes by the *ex situ* process in a DMSO solution followed by crystallization on mp-TiO<sub>2</sub>. Two different types of HTMs, spiro-MeOTAD and PTAA, were used to study the performance of the solar cell devices. Because of the formation of very small (~2–3 nm) MAPbBr<sub>3</sub> perovskite QDs, the current density was drastically increased to 14.07  $\text{mA cm}^{-2}$ . This resulted in an 11.14% conversion efficiency at 1 sun illumination. The resolution of the hysteresis issue is also discussed in detail.

## MATERIALS AND METHODS

### Device fabrication

Laser-patterned FTO-coated glass substrates (TEC-8, Pilkington Group Limited, St Helens, UK, supplied by HANALINTECH, Yongin, South Korea) were ultrasonically cleaned in an alkaline aqueous solution, rinsed with deionized water, ethanol and acetone, and subjected to an O<sub>3</sub> treatment for 30 min. A 20–40-nm-thick compact TiO<sub>2</sub> layer was deposited on the substrates by first spin coating the TiO<sub>2</sub> precursor and then annealing the spin-coated precursor in air at 450 °C for 30 min. The precursor composition was as follows: 0.15 and 0.3 M commercial titanium diisopropoxidebis(acetylacetonate) solution (75% in 2-propanol, Sigma-Aldrich) that was diluted in ethanol (1:39, volume ratio). After cooling the substrates to room temperature, they were treated with the 0.04 M TiCl<sub>4</sub> aqueous solution for 30 min at 70 °C, then rinsed with deionized water and dried at 500 °C for 20 min.

### Deposition of the mesoporous TiO<sub>2</sub> layer

The mp-TiO<sub>2</sub> layer was composed of the 20-nm-sized particles and deposited by spin coating a commercial TiO<sub>2</sub> paste (Dyesol DSL-18NR-T, Dyesol, Queanbeyan, NSW, Australia) diluted in ethanol at 4000 r.p.m. for 15 s. However, the thickness of the mp-TiO<sub>2</sub> layer was optimized using spin-coating speeds from 2500 to 5000 r.p.m. After drying at 125 °C, the TiO<sub>2</sub> films were gradually heated to 500 °C, baked at this temperature for 15 min and then cooled to room temperature. The mesoporous deposited film was again treated with TiCl<sub>4</sub>.

### Preparation of methylammonium lead tribromide ( $\text{CH}_3\text{NH}_3\text{PbBr}_3$ )

Methylammonium lead bromide (MABr) was synthesized by the dropwise addition of hydrobromic acid (HBr) (48 wt% in water, Sigma-Aldrich, St Louis, MO, USA) to a methylamine solution (aqueous, 40 wt%, TCI Chemicals, Tokyo Chemical Industry Co. Ltd., Tokyo, Japan) in an ice bath. The ice-cold solution was stirred for 2 h followed by the solvent evaporation using a rotary evaporator (95 mbar vacuum, 400 r.p.m. rotation) at 60 °C. The resulting white product was dissolved in ethanol and recrystallized using diethyl ether. The fresh fine white crystals were washed three times using diethyl ether and then dried in vacuum for 24 h. The resulting white solid product was used for the  $\text{CH}_3\text{NH}_3\text{PbBr}_3$  synthesis.

The  $\text{CH}_3\text{NH}_3\text{PbBr}_3$  (MAPbBr<sub>3</sub>) precursor solution was prepared by dissolving equimolar amounts of MABr and lead bromide (PbBr<sub>2</sub>) (99.999%, Sigma-Aldrich) in DMSO (Alfa Aesar, Ward Hill, MA, USA) at room temperature overnight. The prepared transparent solution was filtered by a syringe filter (Whatman GD/X PVDF pore size 0.45 μm). The clear transparent solution was dripped onto the top of the mp-TiO<sub>2</sub> film. The film was allowed to soak for 1 min, and then was spun at 1000 r.p.m. for 20 s and 4000 r.p.m. for 30 s. The spin-coated substrate was dried on a hot plate and used for HTM deposition.

The HTM was prepared using a previously reported procedure with a few modifications. We used two different types of HTM for this study. In total, 180 mg of 2,2',7,7'-tetrakis-(*N,N*-di-*p*-methoxyphenyl-amine)-9,9'-spirobifluorene (spiro-MeOTAD, Merck, KGaA Darmstadt, Germany) was dissolved in 1 ml of chlorobenzene (99.8%, Aldrich) with the addition of 37.5 μl bis(trifluoromethane)sulfonimide lithium salt (LiTFSI, 99.95%, Aldrich) (170 mg ml<sup>-1</sup>) in acetonitrile and 17.5 μl 4-*tert*-butylpyridine (96%, Aldrich). For the poly[bis(4-phenyl)(2,4,6-trimethylphenyl)amine] (PTAA)-based HTM,

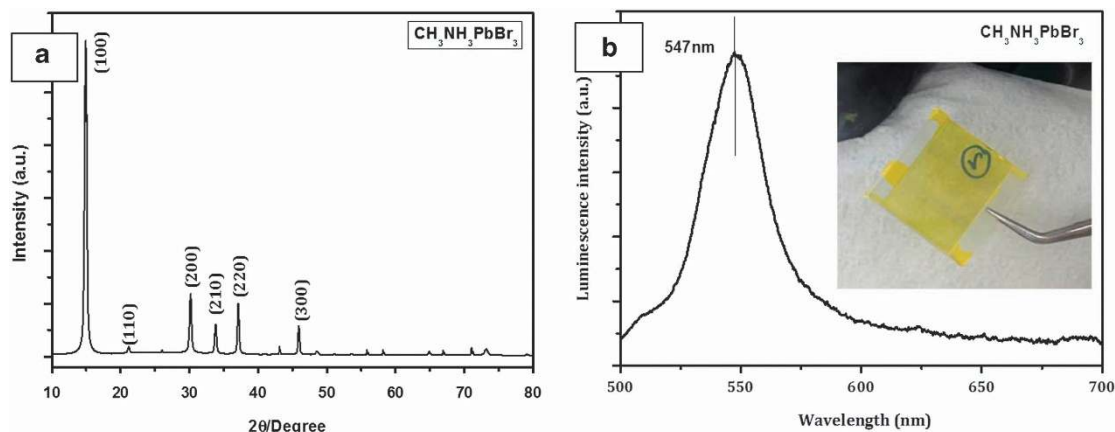


**Figure 1** (a) XRD diffraction pattern of the  $\text{CH}_3\text{NH}_3\text{PbBr}_3$  thin film deposited onto a glass substrate. (b) Corresponding photoluminescence spectrum in the 500–700 nm wavelength range. Inset shows a photograph of the deposited sample.

15 mg of PTAA (EM Index,  $M_w = 17\,500\text{ gmol}^{-1}$ ) in toluene (1.5 ml) was mixed with 15  $\mu\text{l}$  solution of lithium bistrifluoromethanesulfonimide (170 mg) in acetonitrile (1 ml) and 7.5  $\mu\text{l}$  4-tert-butylpyridine. The mixture was spin coated on the FTO/Bi-TiO<sub>2</sub>/mp-TiO<sub>2</sub>+MAPbBr<sub>3</sub> substrates at 3000 r.p.m. for 30 s. Then, the substrates were transferred to a vacuum chamber and evacuated to  $2 \times 10^{-6}$  mbar pressure. For the counter electrode, an 80 nm Au layer was deposited on top of the HTM layer using thermal evaporation (growth rate  $\sim 0.5\text{ \AA s}^{-1}$ ). The active area of the electrode was fixed at 0.09 cm<sup>2</sup>. The active area was calculated using the cross-sectional area of the gold and of the laser pattern.

## RESULTS AND DISCUSSION

The crystalline structure of the synthesized MAPbBr<sub>3</sub> thin film was characterized by X-ray diffraction (XRD) analysis. Figure 1a shows the XRD pattern of the synthesized MAPbBr<sub>3</sub> thin film deposited on a glass substrate. The obtained XRD pattern is consistent with previously reported patterns in the literature.<sup>15,16</sup> The XRD pattern of the MAPbBr<sub>3</sub> sample showed that it had a highly crystalline cubic phase. The lattice parameter of the corresponding cubic phase of the MAPbBr<sub>3</sub> perovskite was found to be  $a = 5.9334(5)\text{ \AA}$  ( $a = 5.94173\text{ \AA}$ , space group =  $Pm\bar{3}m$ ).<sup>25</sup> The Bohr radius of  $\text{CH}_3\text{NH}_3\text{PbBr}_3$  is 20  $\text{\AA}$ .<sup>26,27</sup> Figure 1b shows a typical photoluminescence (PL) spectrum of MAPbBr<sub>3</sub>. The MAPbBr<sub>3</sub> film exhibits an emission peak at 547 nm, which is similar to previously reported observations<sup>28</sup> and is attributed to the NBE emission of MAPbBr<sub>3</sub>.<sup>17</sup>

For the synthesis of the MAPbBr<sub>3</sub> nanoparticles and QDs, we prepared the MAPbBr<sub>3</sub> solution using equimolar amounts of MABr and PbBr<sub>2</sub> in DMSO. The filtered MAPbBr<sub>3</sub>-DMSO solution was dripped onto mp-TiO<sub>2</sub> photoelectrodes and spin coated at a desired speed. We found that the optimized spin-coating process led to the formation of MAPbBr<sub>3</sub> QDs with different sizes. Figure 2a shows a transmission electron microscopy (TEM) micrograph of TiO<sub>2</sub> nanoparticles coated with MAPbBr<sub>3</sub> QDs. The highly magnified TEM image shows that the crystalline mp-TiO<sub>2</sub> nanoparticles are decorated with the crystalline MAPbBr<sub>3</sub> QDs (Figure 2b). The average size of each QD is  $\sim 2\text{--}3\text{ nm}$ , as shown in Figure 2c. Figure 2c also shows a representative high-resolution TEM (HRTEM) image of the MAPbBr<sub>3</sub> QDs and their corresponding fast Fourier transform pattern (inset). These measurements indicate that the nanoparticles have crystalline surfaces without an amorphous layer. We also verified the composition and uniform distribution of the deposited MAPbBr<sub>3</sub> QDs on the mp-TiO<sub>2</sub> surface using scanning transmission electron microscopy (STEM). Elemental mapping was performed using energy

dispersive X-ray analysis (Supplementary Information; Supplementary Figure S1). The HRTEM images show well-defined lattice spacing, and the fast Fourier transform patterns show well-defined spots that match the crystallographic parameters of the MAPbBr<sub>3</sub> QDs and anatase TiO<sub>2</sub>. These results demonstrate that the nanoparticles are highly crystalline and have the same stoichiometry as the bulk.

To study the properties of the nanoparticles in detail, we synthesized different sized MAPbBr<sub>3</sub> perovskites by controlling the experimental conditions. Supplementary Figures S2 show typical TEM/HRTEM analyses of MAPbBr<sub>3</sub>+mp-TiO<sub>2</sub> composites. The experimental techniques section discusses this in greater detail. Initially, we deposited mp-TiO<sub>2</sub> using the spin-coating method. This was used as the base for depositing the MAPbBr<sub>3</sub> nanoparticles. In a typical experiment, we varied the spin-coating speed from 3000 to 5000 r.p.m. In a typical experiment,  $\sim 10\text{ nm}$  MAPbBr<sub>3</sub> perovskite nanoparticles were produced, first by spin coating the MAPbBr<sub>3</sub>-DMSO solution at 2500 r.p.m. (30 s) followed by an additional 30 s cycle at 3000 r.p.m. (Supplementary Figure S2). Supplementary Figure S2a–d shows the TEM/HRTEM analysis of the  $\sim 10\text{ nm}$  MAPbBr<sub>3</sub> nanoparticles. The  $\sim 6\text{--}7\text{ nm}$  MAPbBr<sub>3</sub> perovskite nanoparticles were synthesized by increasing the spin coating rate to 3000 r.p.m. (30 s) and 4500 r.p.m. (30 s) (Supplementary Figure S3). The  $\sim 4\text{--}5\text{ nm}$  MAPbBr<sub>3</sub> QDs were synthesized using the 3000 r.p.m. (10 s) and 5000 r.p.m. (45 s) spin-coating rates (Supplementary Figure S4). The effect of the QD addition was determined by recording the PL spectra for all samples. Supplementary Figure S5 shows the PL spectra of MAPbBr<sub>3</sub> nanoparticle/QDs of different sizes. A small red shift of the emission peak was observed as a function of size of the MAPbBr<sub>3</sub> perovskite QDs.<sup>28,29</sup>

Figure 3 shows the TEM/HRTEM analysis of a MAPbBr<sub>3</sub>+mp-TiO<sub>2</sub> composite. For this sample, the MAPbBr<sub>3</sub>-DMSO solution was first spin cast at 2000 r.p.m. (10 s) and then at 5000 r.p.m. (45 s). Following this, the sample was dried on a hot plate.<sup>30</sup> Figure 3a clearly shows that the mp-TiO<sub>2</sub> nanoparticles formed an inter-connecting nanoparticulate network. Such a network provides a low grain boundary and a fast electron transport. Figure 3b shows a representative highly magnified TEM image of a MAPbBr<sub>3</sub>+mp-TiO<sub>2</sub> composite. It is clear that the TiO<sub>2</sub> surface is decorated with MAPbBr<sub>3</sub> QDs. The average size of the MAPbBr<sub>3</sub> QDs is  $\sim 5\text{ nm}$  (Figure 3c). Furthermore, the MAPbBr<sub>3</sub> QDs have a single phase crystalline nature, as confirmed by the HRTEM analysis (Figure 3d). We used these synthesized MAPbBr<sub>3</sub>

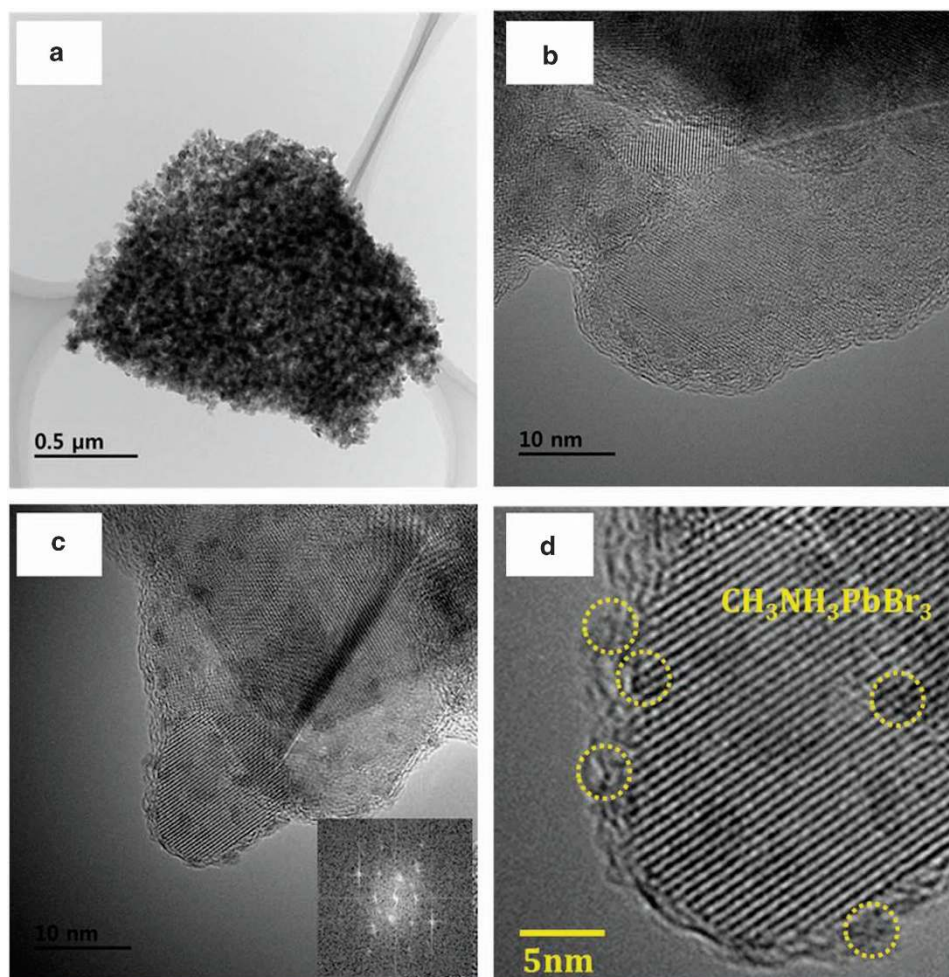


**Figure 2** Structural analysis of mp-TiO<sub>2</sub> coated with CH<sub>3</sub>NH<sub>3</sub>PbBr<sub>3</sub> quantum dots (~2–3 nm). **(a)** TEM micrograph of a CH<sub>3</sub>NH<sub>3</sub>PbBr<sub>3</sub> perovskite deposited on mp-TiO<sub>2</sub> nanoparticles. **(b–c)** Highly magnified TEM images of CH<sub>3</sub>NH<sub>3</sub>PbBr<sub>3</sub>-coated TiO<sub>2</sub> nanoparticles. Inset of **c** shows a fast Fourier transform pattern of CH<sub>3</sub>NH<sub>3</sub>PbBr<sub>3</sub>. **(d)** HRTEM image of CH<sub>3</sub>NH<sub>3</sub>PbBr<sub>3</sub>+mp-TiO<sub>2</sub>.

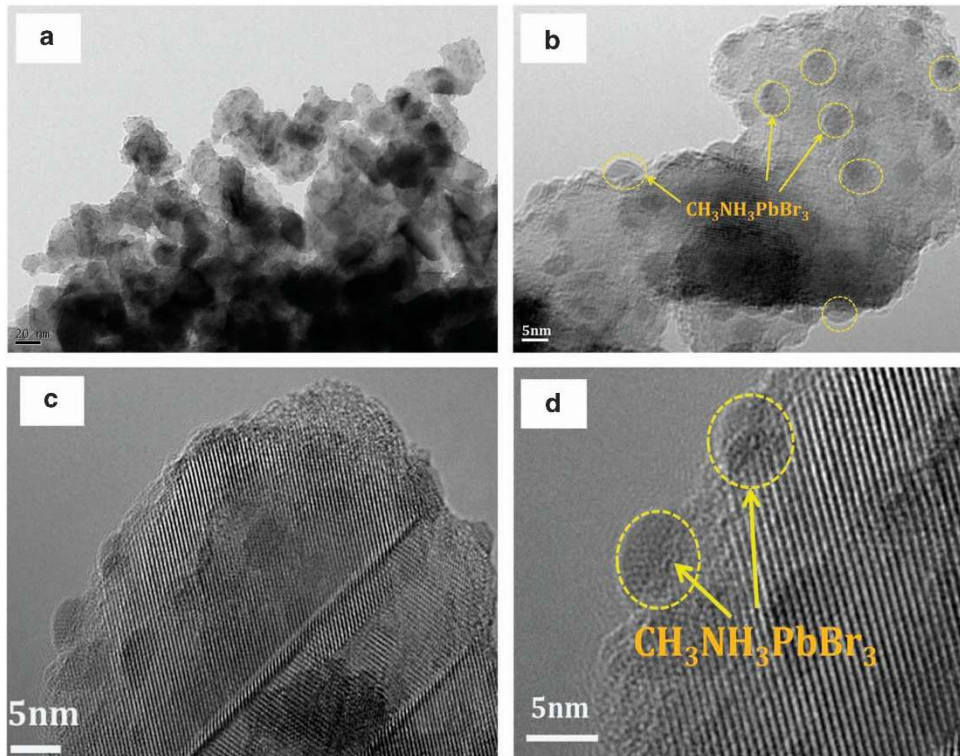
nanoparticles and the QD-decorated mp-TiO<sub>2</sub> nanoparticles to fabricate the solar cell devices.

Figure 4 shows a schematic of the typical device architectures that we used, and the energy level diagrams for the MAPbBr<sub>3</sub>-based solar cells with spiro-MeOTAD and PTAA HTMs. In a typical PSC, the absorber layer (MAPbBr<sub>3</sub>) is sandwiched between the ETL and the hole-transporting layer (HTL). The compact titanium oxide blocking layer (Bi-TiO<sub>2</sub>) with or without the mesoporous scaffold (TiO<sub>2</sub>) acts as the ETL. The HTM (spiro-MeOTAD or PTAA) and the counter electrode (Au, Ag or Al) are the key components of the HTL. The operating principle of the PSC is as follows. When the light illuminates the device the absorbing material (MAPbBr<sub>3</sub>) absorbs the photons to generate the electron–hole pair excitons. Then, the excitons dissociate at the TiO<sub>2</sub>/perovskite interface. The dissociated electrons flow towards the TiO<sub>2</sub> conduction band (CB) to FTO, whereas the holes travel through the HTM layer and reach the Au counter electrode.

The photocurrent density–voltage ( $J$ – $V$ ) characteristics of the fabricated devices were investigated under AM 1.5 G solar irradiance. The average overall photovoltaic performance is presented in Table 1. In this report, we compared two HTMs with different sizes of MAPbBr<sub>3</sub> perovskite as the light absorbing layer (Table 2). Supplementary Figure S6 shows  $J$ – $V$  characteristics of the spiro-MeOTAD HTM-based PSC in the forward and reverse scan modes.

The  $J$ – $V$  measurements were carried out with a 40 ms scanning delay in the reverse (from the open-circuit voltage ( $V_{OC}$ ) to the short-circuit current ( $I_{SC}$ )) and in the forward (that is, from  $I_{SC}$  to  $V_{OS}$ ) modes. The spiro-MeOTAD HTM-based solar cells showed  $V_{OC}$  values in the range of ~0.820–0.910 V. Supplementary Figure S6 shows that all of the tested devices exhibited a  $V_{OC}$  of ~0.900 V. The bulk MAPbBr<sub>3</sub> (~10 nm particle size)-based devices show a short-circuit current density ( $J_{SC}$ ) of 8.15 mA cm<sup>-2</sup>, an open-circuit voltage ( $V_{OC}$ ) of 0.888 V and a FF of 0.54, resulting in a PCE of 3.91%. The MAPbBr<sub>3</sub>-based perovskite devices with ~7–8 nm particle sizes show a 4.22% conversion efficiency with the following parameters:  $J_{SC}$  = 8.97 mA cm<sup>-2</sup>, FF = 0.54 and  $V_{OC}$  = 0.873 V. By contrast, the MAPbBr<sub>3</sub> devices with 5–7 nm particle sizes have the following characteristics:  $V_{OC}$  = 0.894 V,  $J_{SC}$  = 9.79 mA cm<sup>-2</sup>, FF = 0.52, resulting in a PCE of 4.55% in the reverse scan mode. However, these devices have 3.02, 4.04 and 4.45% PCE values in forward scan direction for the 10, 7 and 5 nm, respectively (Supplementary Table S1).

A similar trend was observed for the PTAA-based MAPbBr<sub>3</sub> solar cell devices (Supplementary Table S2). All devices show  $V_{OC}$  values between 1.000 and 1.100 V. MAPbBr<sub>3</sub> solar cells without QDs show lower PCE (up to 4.40%) (Supplementary Figure S7). The 7–8 nm MAPbBr<sub>3</sub>-based devices show the following characteristics:  $J_{SC}$  = 9.44 mA cm<sup>-2</sup>, FF = 0.58 and  $\eta$  = 5.73%. The 5–7 nm MAPbBr<sub>3</sub>



**Figure 3** TEM analysis of a  $\text{CH}_3\text{NH}_3\text{PbBr}_3$ + $\text{mp-TiO}_2$  composite with  $\sim 5$  nm  $\text{CH}_3\text{NH}_3\text{PbBr}_3$  particle sizes. (a) TEM micrograph of a  $\text{CH}_3\text{NH}_3\text{PbBr}_3$  perovskite deposited on  $\text{mp-TiO}_2$  interconnected nanoparticles. (b–c) Highly magnified TEM images of  $\text{CH}_3\text{NH}_3\text{PbBr}_3$ -coated  $\text{TiO}_2$  nanoparticles. (d) HRTEM image of  $\text{CH}_3\text{NH}_3\text{PbBr}_3$  QDs, which are denoted by the yellow dotted circles.

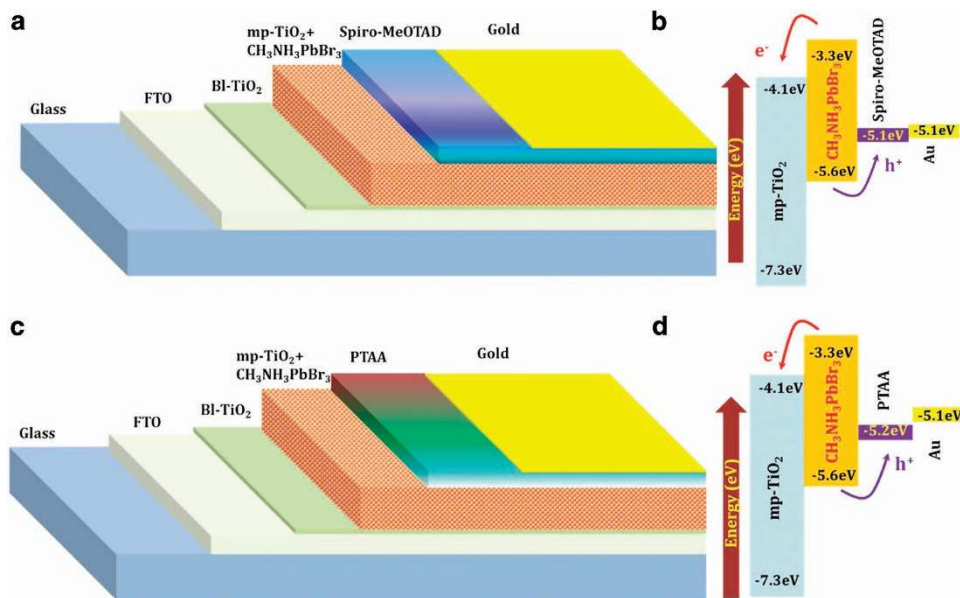


**Figure 4** Device configurations and energy level diagrams of  $\text{CH}_3\text{NH}_3\text{PbBr}_3$ -based perovskite solar cells used in this study. (a–b) Spiro-MeOTAD-based devices. (c–d) PTAA. The energy level values are obtained from the published literature.

nanoparticle-based samples exhibited the following characteristics:  $V_{\text{OC}}=1.082$  V,  $J_{\text{SC}}=10.85$   $\text{mA cm}^{-2}$ ,  $\text{FF}=0.59$  and a 6.93% conversion efficiency (Supplementary Table S2).

However, all of these devices show low FF, and the high hysteresis behavior observed might be due to the thickness of the  $\text{mp-TiO}_2$  layer.<sup>17</sup> Therefore, we optimized the thickness of  $\text{mp-TiO}_2$  by varying the spin-coating speed. Supplementary Figure S8 shows the cross-

sectional micrographs of a  $\text{mp-TiO}_2$ + $\text{MAPbBr}_3$  composite deposited at various spinning rates. From the cross-sectional field emission scanning electron microscopy micrographs, we observed that the thickness of the  $\text{mp-TiO}_2$  layer that was deposited at 2500, 3000, 4000 and 5000 r.p.m. was 533, 423, 364 and 279 nm, respectively. Furthermore, we verified the uniformity of the layer for the HTM deposition for the respective photoelectrodes. The inset micrographs

**Table 1** Average solar cell properties of the optimized  $\text{MAPbBr}_3$  quantum dot-based (~5 nm) perovskite solar cells

HTM	Scan		$V_{OC}$ (V)	$J_{SC}$ ( $\text{mA cm}^{-2}$ )	FF	$\eta$ (%)
	direction					
Spiro-MeOTAD	Forward		$0.941 \pm 0.01$	$10.39 \pm 0.35$	$0.63 \pm 0.01$	6.15
	Reverse		$0.928 \pm 0.01$	$10.54 \pm 0.52$	$0.66 \pm 0.01$	6.45
PTAA	Forward		$1.005 \pm 0.01$	$11.12 \pm 0.45$	$0.53 \pm 0.01$	5.92
	Reverse		$1.042 \pm 0.01$	$10.86 \pm 0.34$	$0.63 \pm 0.01$	7.13

Abbreviations: FF, fill factor; HTM, hole-transporting material; PTAA, poly[bis(4-phenyl)(2,4,6-trimethylphenyl)amine]; Spiro-MeOTAD, 2,2',7,7'-tetrakis-(N,N-di-4-methoxyphenylamino)-9,9'-spirobifluorene. Thickness of the mp-TiO<sub>2</sub> electrode is 250 nm. All measurements were performed at room temperature without masking. The device configuration was FTO/BI-TiO<sub>2</sub>/mp-TiO<sub>2</sub>/CH<sub>3</sub>NH<sub>3</sub>PbBr<sub>3</sub>/HTM/Au.

**Table 2** Average solar cell properties of the optimized  $\text{MAPbBr}_3$  quantum dot-based (~2–3 nm) perovskite solar cells

HTM	Scan		$V_{OC}$ (V)	$J_{SC}$ ( $\text{mA cm}^{-2}$ )	FF	$\eta$ (%)
	direction					
Spiro-MeOTAD	Forward		$0.951 \pm 0.01$	$11.68 \pm 0.35$	$0.69 \pm 0.01$	7.66
	Reverse		$0.932 \pm 0.01$	$11.50 \pm 0.52$	$0.71 \pm 0.01$	7.61
PTAA	Forward		$1.097 \pm 0.01$	$12.31 \pm 0.45$	$0.69 \pm 0.01$	9.31
	Reverse		$1.089 \pm 0.01$	$12.05 \pm 0.34$	$0.72 \pm 0.01$	9.44

Abbreviations: FF, fill factor; HTM, hole-transporting material; PTAA, poly[bis(4-phenyl)(2,4,6-trimethylphenyl)amine]; Spiro-MeOTAD, 2,2',7,7'-tetrakis-(N,N-di-4-methoxyphenylamino)-9,9'-spirobifluorene. Thickness of the mp-TiO<sub>2</sub> electrode is 250 nm. All measurements were performed at room temperature without masking. The device configuration was FTO/BI-TiO<sub>2</sub>/mp-TiO<sub>2</sub>/CH<sub>3</sub>NH<sub>3</sub>PbBr<sub>3</sub>/HTM/Au.

show the top view of mp-TiO<sub>2</sub>+MAPbBr<sub>3</sub> covered with the HTM material. These micrographs confirmed that the HTM uniformity on the mp-TiO<sub>2</sub>+MAPbBr<sub>3</sub> composite increased with a higher spin-coating rate. A complete pin hole-free coverage of the HTM (spiro-MeOTAD or PTAA) was achieved at a spin coat speed of 5000 r.p.m. The HTM layer uniformity helps to increase the  $V_{OC}$  and FF parameters of the device.

Figure 5 shows typical  $J-V$  plots in forward and reverse scan modes for  $\text{MAPbBr}_3$  with ~5 nm particle sizes. The FTO/BI-TiO<sub>2</sub>/mp-TiO<sub>2</sub>+MAPbBr<sub>3</sub> (~5 nm)/spiro-MeOTAD/Au-based perovskite exhibits a PCE of 6.15% and 6.45% for the forward and reverse scan, respectively. For the standard spiro-MeOTAD-based devices, the forward scan exhibits the following characteristics:  $V_{OC}$ =0.941 V,  $J_{SC}$ =10.39 mA cm<sup>-2</sup>, FF=0.63 and  $\eta$ =6.15%. The reverse scan shows similar values: PCE=6.45% ( $V_{OC}$ =0.928 V,  $J_{SC}$ =10.54 mA cm<sup>-2</sup> and FF=0.66). The PTAA-based devices show a 5.92 and 7.13% PCE for the forward and reverse scan modes, respectively. This sample shows high hysteresis behavior. Therefore, we optimized the conditions of the BI-TiO<sub>2</sub> layer deposition and the thickness of the mp-TiO<sub>2</sub> layer. The BI-TiO<sub>2</sub> layer was deposited by spin coating the 0.15 M solution twice followed by spin coating the 0.3 M solution once. The sample was annealed at 500 °C and treated with TiCl<sub>4</sub>. The mp-TiO<sub>2</sub> layer was deposited at 5000 r.p.m. and the MAPbBr<sub>3</sub>-DMSO solution was spin cast at 1000 (10 s) and 5000 (45 s) r.p.m., respectively. Figure 6 shows typical  $J-V$  plots of the optimized ~2–3 nm  $\text{MAPbBr}_3$  QD devices that are based on spiro-MeOTAD and PTAA HTMs in forward and reverse scan modes. The FTO/BI-TiO<sub>2</sub>/mp-TiO<sub>2</sub>+MAPbBr<sub>3</sub>(≤3 nm)/spiro-MeOTAD/Au-based perovskite exhibits a PCE of 7.66 and 7.61% for the forward and reverse scan modes,

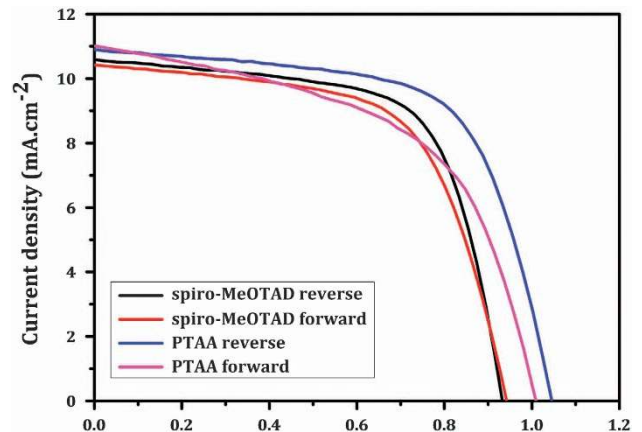


**Figure 5**  $J-V$  curves of the forward and reverse bias sweeps and the respective  $J-V$  curves for spiro-MeOTAD and PTAA that have a  $\text{CH}_3\text{NH}_3\text{PbBr}_3$  perovskite absorber layer of ~5-nm-sized particle.  $J-V$  curves were measured using forward and reverse scans with 10 mV voltage steps and 50 ms delay times under AM 1.5 G illumination.

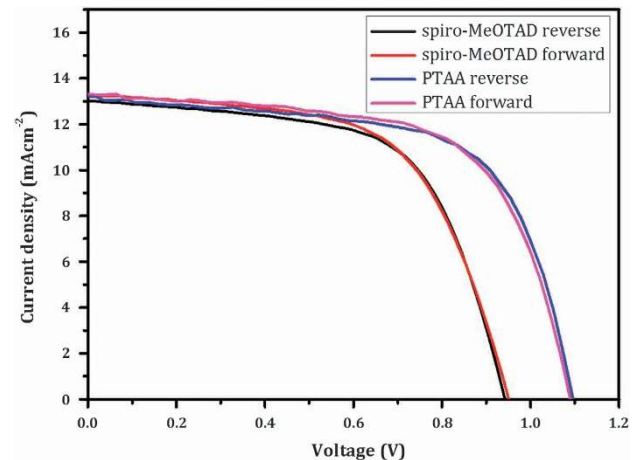


**Figure 6**  $J-V$  curves of forward and reverse bias sweeps and respective  $J-V$  curves for spiro-MeOTAD and PTAA that have a  $\text{CH}_3\text{NH}_3\text{PbBr}_3$  perovskite (~2–3 nm) absorber layer.  $J-V$  curves were measured using forward and reverse scans with 10 mV voltage steps and 50 ms delay times under AM 1.5 G illumination.

respectively. In case of the standard spiro-MeOTAD-based devices, the forward scan exhibits the following parameters:  $V_{OC}$ =0.951 V,  $J_{SC}$ =11.68 mA cm<sup>-2</sup>, FF=0.69 and  $\eta$ =7.66%. The reverse scan shows similar characteristics: PCE=7.61% ( $V_{OC}$ =0.932 V,  $J_{SC}$ =11.50 mA cm<sup>-2</sup> and FF=0.71). Little improvement in the FF was observed but this did not significantly affect the PCE. Furthermore, we studied the effect of the forward and reverse scan for the FTO/BI-TiO<sub>2</sub>/mp-TiO<sub>2</sub>+MAPbBr<sub>3</sub>/PTAA/Au-based PSCs, as shown in Figure 6. The  $J_{SC}$ ,  $V_{OC}$  and FF values that were obtained from the  $J-V$  curves of the forward scan were 12.31 mA cm<sup>-2</sup>, 1.097 V and 0.69, respectively, thus, yielding a PCE of 9.31%. By contrast, the corresponding values from the  $J-V$  curve of the reverse scan were  $J_{SC}$ =12.05 mA cm<sup>-2</sup>,  $V_{OC}$ =1.089 V and FF=0.72, thus, yielding a 9.44% conversion efficiency. The reverse scan demonstrated a drastic improvement in the FF results and in the 9.44% PCE. Overall, the forward and reverse scans exhibited almost similar efficiency, which indicates that each layer of these devices was optimized well.<sup>18</sup> The above observations demonstrate that the  $V_{OC}$  was drastically improved

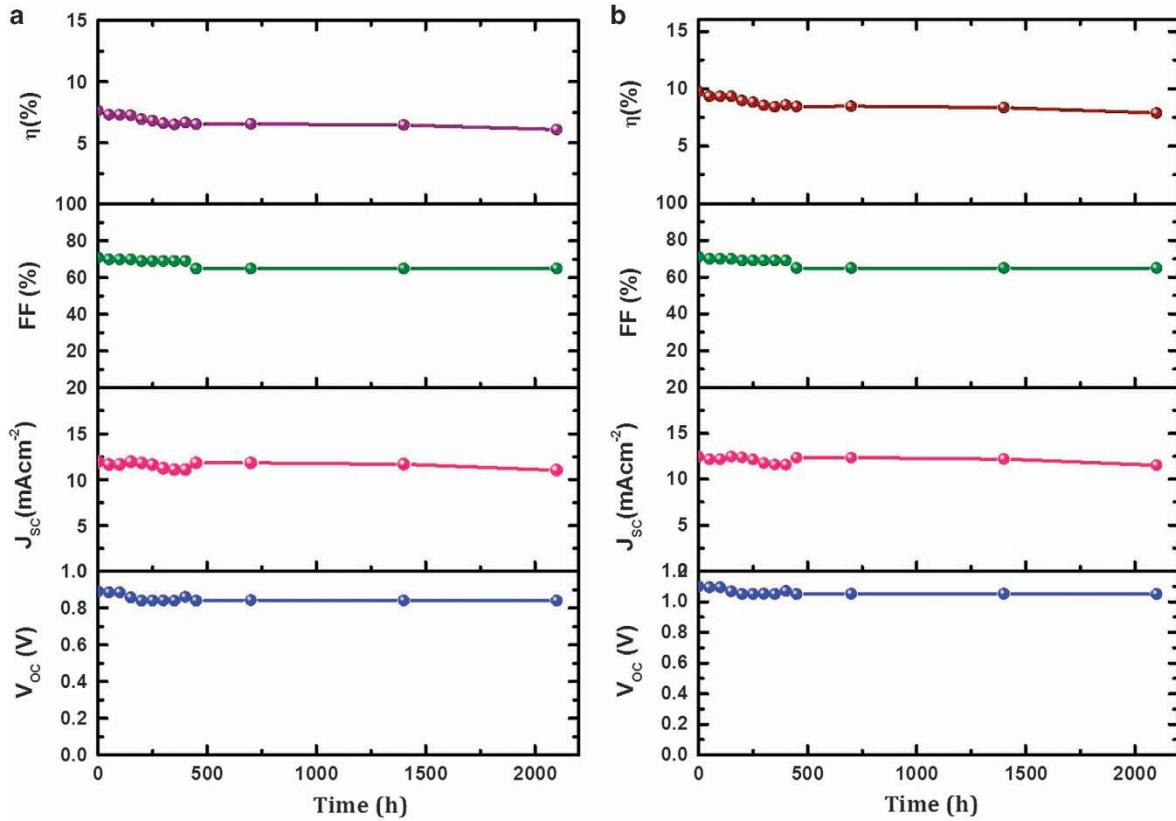


**Figure 7** Stability measurements of  $\text{CH}_3\text{NH}_3\text{PbBr}_3$  nanoparticle-based perovskite solar cells. (a) FTO/BI-TiO<sub>2</sub>/mp-TiO<sub>2</sub>+CH<sub>3</sub>NH<sub>3</sub>PbBr<sub>3</sub>/spiro-MeOTAD/Au. (b) FTO/BI-TiO<sub>2</sub>/mp-TiO<sub>2</sub>+CH<sub>3</sub>NH<sub>3</sub>PbBr<sub>3</sub>/PTAA/Au.

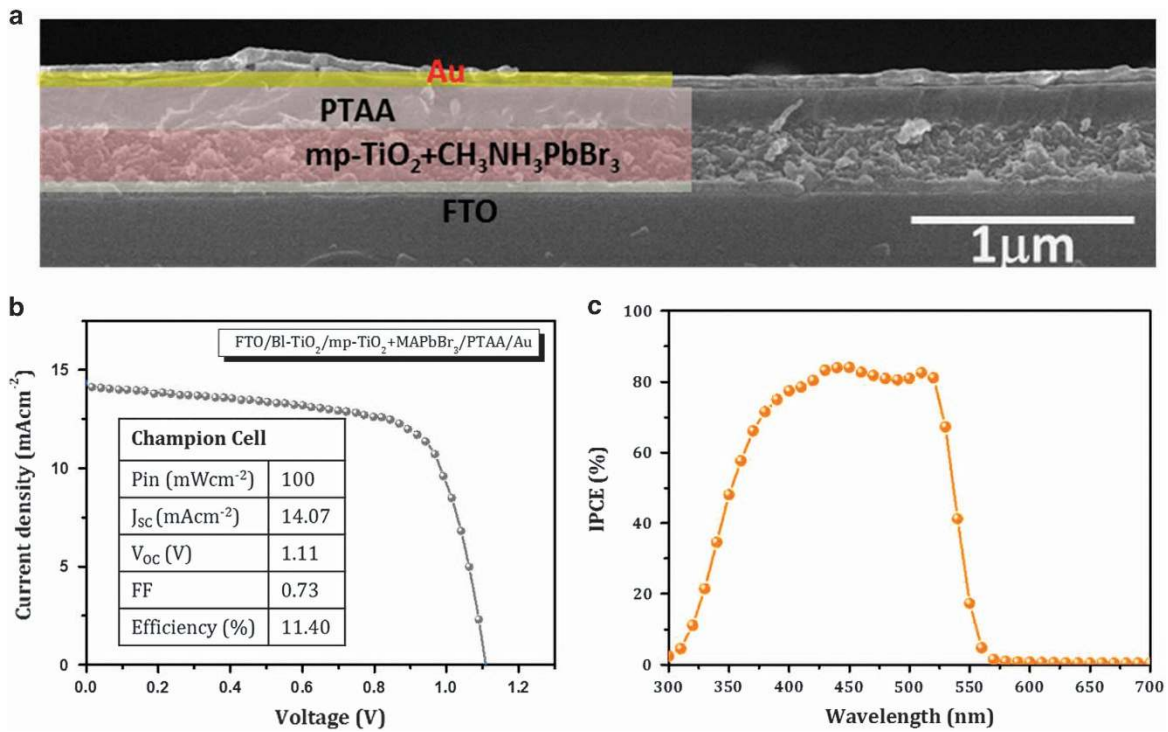


**Figure 8** Solar cell properties of the champion cell with a FTO/BI-TiO<sub>2</sub>/mp-TiO<sub>2</sub>+CH<sub>3</sub>NH<sub>3</sub>PbBr<sub>3</sub>/PTAA/Au device configuration. (a) Cross-sectional field emission scanning electron microscopy image of a fabricated perovskite solar cell device. (b) Photocurrent density–voltage ( $J$ - $V$ ) curve and (c) incident power conversion efficiency (IPCE) spectrum of the champion cell.

(up to 1.097 V) due to the level of the highest occupied molecular orbital (HOMO) of PTAA ( $-5.2$  eV) rather than spiro-MeOTAD ( $-5.1$  eV). The PTAA-based device showed high conversion efficiency. Interestingly, the current density increased slightly ( $12.31$  mA  $\text{cm}^{-2}$ ), whereas the  $V_{\text{OC}}$  increased drastically up to 1.097 V compared with spiro-MeOTAD. Therefore, the PTAA device shows higher conversion efficiency than the spiro-MeOTAD device. Analysis of the HOMO level of both HTMs showed that PTAA exhibits a slightly higher HOMO level. This facilitates the  $V_{\text{OC}}$  increase. Moreover, there is little difference among the following parameters: (1) valence band maximum of MAPbBr<sub>3</sub> and the HOMO level of PTAA in comparison with spiro-MeOTAD; (2) the large offset between the conduction band minimum of MAPbBr<sub>3</sub> and the quasi-Fermi levels of TiO<sub>2</sub>; and (3) the possible interaction between TiO<sub>2</sub>/MAPbBr<sub>3</sub>/PTAA. In addition, the hole mobility of PTAA (P-type (mobility =  $10^{-3}$ – $10^{-2}$  cm<sup>2</sup> V<sup>-1</sup> s))<sup>31</sup> is much higher than spiro-MeOTAD ( $2 \times 10^{-4}$  cm<sup>2</sup> V<sup>-1</sup> s).<sup>32–34</sup> Therefore, the current density also increases. Supplementary Figure S9 depicts the PCE dependence on MAPbBr<sub>3</sub> particle size with different HTMs. Figure 7 shows the air stability of the fabricated perovskite devices. For the stability evaluation, we stored the devices in an Al foil-covered Petri dish in air at room temperature without encapsulation. The  $V_{\text{OC}}$  and  $J_{\text{SC}}$  values of both devices were stable for up to 2500 h, after which a slight decline was observed.

Figure 8a shows a typical cross-sectional field emission scanning electron microscopy image of the fabricated device. The appropriate thickness of each layer confirms that the optimized device has 250 nm of mp-TiO<sub>2</sub> with  $\leq 3$  nm of MAPbBr<sub>3</sub> QDs and 180 nm of the HTM layer and 80 nm of the gold contact. The highly magnified TEM image shows that the surface of mp-TiO<sub>2</sub> is well coated with the MAPbBr<sub>3</sub> particles (Figure 2c). Figure 8b shows the  $J$ – $V$  curve of the champion cell that was recorded for the MAPbBr<sub>3</sub> perovskite. This layer was deposited with little variation according to our previous method. The MAPbBr<sub>3</sub>–DMSO solution was dripped onto mp-TiO<sub>2</sub>, allowed to soak for  $\sim 30$  s, and then spin coated. The spin-coating speed was maintained at 1000 r.p.m. and at 5000 r.p.m. for 10 and 40 s, respectively. The deposited sample was dried on a hot plate to evaporate the solvent and to crystallize MAPbBr<sub>3</sub>. The dried mp-TiO<sub>2</sub>+MAPbBr<sub>3</sub> photoelectrodes were used for the PTAA deposition. The PTAA HTM layer was deposited at 3500 r.p.m. for 30 s and 80 nm gold fingers were deposited using thermal evaporation. For the champion cell, the highest PCE of 11.41% was achieved because of the high  $V_{\text{OC}} = 1.110$  V and the high current density of 14.07 mA  $\text{cm}^{-2}$ . It was observed that the FF = 0.73 was also much higher than for the other samples tested. This enhancement was primarily due to the lower back reaction, lower recombination rate, high FF and high current density. To confirm this observation, we also recorded the incident photon-to-electron conversion efficiency (IPCE) data. Figure 8c shows the IPCE spectra as a function of the wavelength of the champion cell. The IPCE spectra provide detailed information on the effective light harvesting capabilities of the perovskite-based solar cells. The photocurrent generation starts at  $\sim 550$  nm, which is in agreement with the band gap of  $\text{CH}_3\text{NH}_3\text{PbBr}_3$ , and reaches up to  $\sim 82\%$  IPCE in the visible spectrum.

## CONCLUSIONS

In summary, we synthesized methylammonium lead bromide MAPbBr<sub>3</sub> QDs via a DMSO solvent-based method and used these QDs to fabricate PSCs with different HTMs. Fabrication of MAPbBr<sub>3</sub> perovskite of different particle sizes was controlled by the experimental conditions. The photovoltaic performance was significantly dependent on the size of the MAPbBr<sub>3</sub> nanoparticles and QDs. The best con-

version efficiency of 11.46% ( $V_{\text{OC}} = 1.110$  V,  $J_{\text{SC}} = 14.07$  mA  $\text{cm}^{-2}$ ) was achieved with PTAA as the HTM and a 0.73 FF for the  $\leq 3$  nm MAPbBr<sub>3</sub> QDs. This solar cell performance enhancement was attributed to the MAPbBr<sub>3</sub> QDs having sizes  $\leq 3$  nm. This result enables us to elucidate the perovskite operating mechanism. The hysteresis study revealed that the MAPbBr<sub>3</sub>-based cells show a very low tolerance towards the  $\sim 250$  nm mp-TiO<sub>2</sub> thickness. We believe that our method can be applied to achieve stable planar hybrid PSCs. The implementation of MAPbI<sub>3</sub> and MAPbBr<sub>3</sub> QDs will also open new opportunities for the development of efficient PSCs. Such studies, based on different HTMs, are currently underway in our laboratory.

## CONFLICT OF INTEREST

The authors declare no conflict of interest.

## ACKNOWLEDGEMENTS

This research was supported by the Basic Science Research Program through the National Research Foundation of Korea (NRF) that was funded by the Ministry of Education (NRF-2009-0094055). This research work was also supported by Basics Science Research Program through the National Foundation of Korea (NRF) funded by the Ministry of Education (NRF-2014R1A2054051)

*Author contributions:* SSM and CKH conceived and designed the experiments, analyzed the data and wrote the manuscript. SSM carried out all of the experiments and wrote the manuscript. SSM and CSS performed the mp-TiO<sub>2</sub> and TiCl<sub>4</sub> treatment. All authors discussed the results and reviewed the manuscript.

- Wells, H. L. Über die Cäsium- und Kalium-Bleihalogenide. *Z. Anorg. Chem.* **3**, 195–210 (1893).
- Poglitich, A. & Weber, D. Dynamic disorder in methylammoniumtrihalogenoplumbates (II) observed by millimeter-wave spectroscopy. *J. Chem. Phys.* **87**, 6373–6378 (1987).
- MÖLLER, C. K. Crystal structure and photoconductivity of cesium plumbohalides. *Nature* **182**, 1436 (1958).
- Suarez, B., Gonzalez-Pedro, V., Ripolles, T. S., Sanchez, R. S., Otero, L. & Mora-Sero, I. Recombination study of combined halides (Cl, Br, I) perovskite solar cells. *J. Phys. Chem. Lett.* **5**, 1628–1635 (2014).
- Jang, D. M., Park, K., Kim, D. H., Park, J., Shojaei, F., Kang, H. S., Ahn, J.-P., Lee, J. W. & Song, J. K. Reversible halide exchange reaction of organometal trihalide perovskite colloidal nanocrystals for full-range band gap tuning. *Nano Letter* (e-pub ahead of print 10 July 2015; doi:10.1021/acs.nanolett.5b01430).
- Im, J.-H., Lee, C.-R., Lee, J.-W., Park, S.-W. & Park, N. G. 6.5% Efficient perovskite quantum-dot-sensitized solar cell. *Nanoscale* **3**, 4088–4093 (2011).
- Burschka, J., Pellet, N., Moon, S. J., Humphry-Baker, R., Gao, P., Nazeeruddin, M. K. & Grätzel, M. Sequential deposition as a route to high-performance perovskite-sensitized solar cells. *Nature* **499**, 316–319 (2013).
- Zhou, H., Chen, Q., Li, G., Luo, S., Song, T., Duan, H.-S., Hong, Z., You, J., Liu, Y. & Yang, Y. Interface engineering of highly efficient perovskite solar cells. *Science* **345**, 542–546 (2014).
- Liu, M., Johnston, M. B. & Snaith, H. J. Efficient planar heterojunction perovskite solar cells by vapour deposition. *Nature* **501**, 395–398 (2013).
- Stranks, S. D., Eperon, G. E., Grancini, G., Menelaou, C., Alcocer, M. J. P., Leijtens, T., Herz, L. M., Petrozza, A. & Snaith, H. J. Electron-hole diffusion lengths exceeding 1 micrometer in an organometal trihalide perovskite absorber. *Science* **342**, 341–344 (2013).
- Lee, M. M., Teuscher, J., Miyasaka, T., Murakami, T. N. & Snaith, H. J. Efficient hybrid solar cells based on meso-structured organometal halide perovskites. *Science* **338**, 643 (2012).
- Hu, Y. H. Novel meso-structured solar cells (MSSCs) with a high efficiency exceeding 12%. *Adv. Mater.* **26**, 2102 (2014).
- Mali, S. S., Shim, C. S., Patil, P. S. & Hong, C. K. Once again, organometallic tri-halide perovskites: Efficient light harvester for solid state perovskite solar cells. *Mater. Today* **18**, 172–173 (2015).
- Mali, S. S., Shim, C. S., Park, H. K., Heo, J., Patil, P. S. & Hong, C. K. Ultrathin atomic layer deposited TiO<sub>2</sub> for surface passivation of hydrothermally grown 1D TiO<sub>2</sub> nanorod arrays for efficient solid-state perovskite solar cells. *Chem. Mater.* **27**, 1541–1551 (2015).
- You, J., Hong, Z., Yang, Y., Chen, Q., Cai, M., Song, T.-B., Chen, C.-C., Lu, S., Liu, Y., Zhou, H. & Yang, Y. Low-temperature solution-processed perovskite solar cells with high efficiency and flexibility. *ACS Nano* **8**, 1674–1680 (2014).

- 16 Seo, J., Park, S., Kim, Y. C., Jeon, N. J., Noh, J. H., Yoon, S. C. & Seok, S. I. Benefits of very thin PCBM and LiF layers for solution-processed p–i–n perovskite solar cells. *Energy Environ. Sci.* **7**, 2642–2646 (2014).
- 17 Jeon, N. J., Noh, J. H., Kim, Y. C., Yang, W. S., Ryu, S. & Seok, S. I. Solvent engineering for high-performance inorganic–organic hybrid perovskite solar cells. *Nat. Mater.* **13**, 897–903 (2014).
- 18 Jeon, N. J., Noh, J. H., Yang, W. S., Kim, Y. C., Ryu, S., Seo, J. & Seok, S. I. Compositional engineering of perovskite materials for high-performance solar cells. *Nature* **517**, 476–480 (2015).
- 19 Schmidt, L. C., Pertegas, A., González-Carrero, S., Malinkiewicz, O., Agouram, S., Espallargas, G. M., Bolink, H. J., Galian, R. E. & Pérez-Prieto, J. Nontemplate synthesis of CH<sub>3</sub>NH<sub>3</sub>PbBr<sub>3</sub> perovskite nanoparticles. *J. Am. Chem. Soc.* **136**, 850–853 (2014).
- 20 Heo, J. H., Song, D. H. & Im, S. H. Planar CH<sub>3</sub>NH<sub>3</sub>PbBr<sub>3</sub> hybrid solar cells with 10.4% power conversion efficiency, fabricated by controlled crystallization in the spin-coating process. *Adv. Mater.* **26**, 8179–8183 (2014).
- 21 Tanaka, K., Takahashi, T., Ban, T., Kondo, T., Uchida, K. & Miura, N. Comparative study on the excitons in lead-halide-based perovskite-type crystals CH<sub>3</sub>NH<sub>3</sub>PbBr<sub>3</sub> CH<sub>3</sub>NH<sub>3</sub>PbI<sub>3</sub>. *Solid State Commun.* **127**, 619–623 (2003).
- 22 Cai, B., Xing, Y., Yang, Z., Zhang, W. H. & Qiu, J. High performance hybrid solar cells sensitized by organo lead halide perovskites. *Energy Environ. Sci.* **6**, 1480–1485 (2013).
- 23 Edri, E., Kirmayer, S., Cahen, D. & Hodes, G. High open-circuit voltage solar cells based on organic–inorganic lead bromide perovskite. *J. Phys. Chem. Lett.* **4**, 897–902 (2013).
- 24 Noh, J. H., Hyuklm, S., Heo, J. H., Mandal, T. N. & Seok, S. I. Chemical management for colorful efficient and stable inorganic–organic hybrid nanostructured solar cells. *Nano Lett.* **13**, 1764–1769 (2013).
- 25 Ryu, S., Noh, J. H., Jeon, N. J., Kim, Y. C., Yang, W. S., Seo, J. & Seok, S. I. Voltage output of efficient perovskite solar cells with high open-circuit voltage and fill factor. *Energy Environ. Sci.* **7**, 2614–2618 (2014).
- 26 Liu, C., Qiu, Z., Meng, W., Chen, J., Qi, J., Dong, C. & Wang, M. Effects of interfacial characteristics on photovoltaic performance in CH<sub>3</sub>NH<sub>3</sub>PbBr<sub>3</sub>-based bulk perovskite solar cells with core/shell nanoarray as electron transporter. *Nano Energy* **12**, 59–68 (2015).
- 27 Koutselas, I. B., Ducasse, L. & Papavassiliou, G. C. Electronic properties of three- and low-dimensional semiconducting materials with Pb halide and Sn halide units. *J. Phys. Condens. Matter* **8**, 1217 (1996).
- 28 Zhang, M., Yu, H., Lyu, M., Wang, Q., Yun, J.-H. & Wang, L. Composition-dependent photoluminescence intensity and prolonged recombination lifetime of perovskite CH<sub>3</sub>NH<sub>3</sub>PbBr<sub>3-x</sub>Cl<sub>x</sub> films. *Chem. Commun.* **50**, 11727–11730 (2014).
- 29 Nie, W., Tsai, H., Asadpour, R., Blancon, J.-C., Neukirch, A. J., Gupta, G., Crochet, J. J., Chhowalla, M., Tretiak, S., Alam, M. A., Wang, H. L. & Mohite, A. D. High-efficiency solution-processed perovskite solar cells with millimeter-scale grains. *Science* **347**, 522–525 (2015).
- 30 Aldibaja, F. K., Badia, L., Mas-Marza, E., Sanchez, R. S., Barea, E. M. & Mora-Sero, I. Effect of different lead precursors on perovskite solar cell performance and stability. *J. Mater. Chem. A* **3**, 9194–9200 (2015).
- 31 Heo, J. H., Im, S. H., Noh, J. H., Mandal, T. N., Lim, C.-S., Chang, J. A., Lee, Y. H., Kim, H.-J., Sarkar, A., Nazeeruddin, M. K., Grätzel, M. & Seok, S. I. Efficient inorganic–organic hybrid heterojunction solar cells containing perovskite compound and polymeric hole conductors. *Nat. Photonics* **7**, 486–491 (2013).
- 32 Snaith, H. J. & Grätzel, M. Electron and Hole Transport through Mesoporous TiO<sub>2</sub> Infiltrated with Spiro-MeOTAD. *Adv. Mater.* **19**, 3643–3647 (2007).
- 33 Leijtens, T., Ding, I.-K., Giovenzana, T., Bloking, J. T., McGehee, M. D. & Sellinger, A. Hole transport materials with low glass transition temperatures and high solubility for application in solid-state dye-sensitized solar cells. *ACS Nano* **6**, 1455–1462 (2012).
- 34 Poplavskyy, D. & Nelson, J. Nondispersive hole transport in amorphous films of methoxy-spirofluorene-arylamine organic compound. *J. Appl. Phys.* **93**, 341 (2003).



This work is licensed under a Creative Commons Attribution 4.0 International License. The images or other third party material in this article are included in the article's Creative Commons license, unless indicated otherwise in the credit line; if the material is not included under the Creative Commons license, users will need to obtain permission from the license holder to reproduce the material. To view a copy of this license, visit <http://creativecommons.org/licenses/by/4.0/>

Supplementary Information accompanies the paper on the NPG Asia Materials website (<http://www.nature.com/am>)